RSC Advances

PAPER

View Article Online
View Journal | View Issue

Cite this: *RSC Adv.*, 2018, **8**, 16657

Flexible C–Mo_2C fiber film with self-fused junctions as a long cyclability anode material for sodium-ion battery†

Wenjie Zhang,[a] Zeyu Guo,[a] Qinghua Liang,[a] Ruitao Lv,[ab] Wanci Shen,[a] Feiyu Kang,[a] Yuqing Weng[a] and Zheng-Hong Huang *[ab]

Received 4th March 2018
Accepted 9th April 2018

DOI: 10.1039/c8ra01908h

rsc.li/rsc-advances

Electrospun carbon fiber films have high contact resistance at the fiber junctions, which causes poor cycling stability and limits their further improvement in energy storage performances. To eliminate the contact resistance of the film, we provide a new strategy to fuse the fiber junctions by introducing MoO_2 in the fibers, which replaces the C–C interface by a more active C–MoO_2–C interface at the fiber junction to promote mass transfer. MoO_2 reacts with C matrix to generate Mo_2C and form self-fused junctions during the carbonization process. Due to much lower charge transfer and sodium diffusion resistance, the C–Mo_2C fiber film with self-fused junctions shows much better cyclability with capacity retention of 90% after 2000 cycles at a constant current density of 1 A g^{-1}. Moreover, the Mo_2C particles provide many electrochemically active sites, leading to additional improvement in sodium storage. The C–Mo_2C fiber film has a capacity of 134 mA h g^{-1} at 1 A g^{-1} and a high capacity of 99 mA h g^{-1} even at 5 A g^{-1}.

1. Introduction

As the demand for better rechargeable batteries keeps increasing, one of the major challenges is to provide low cost and environmentally friendly high power energy resources. Sodium-ion batteries (SIBs) have attracted much attention because of the abundance and low cost of sodium.[1,2] SIBs have shown potential to occupy the market for large-scale energy storage, in particular for smart electric grids.[3–6] However, the graphite anode used in LIBs is not suitable for sodium-ion storage because of the weak interaction between Na and C and the large ionic radius of sodium.[7,8] Hard-carbon materials with low graphitization have proven to be more suitable for Na^+ storage because of their large interlayer distance and disordered structure.[7,9–11] Among the hard-carbon materials, electrospun carbon fiber films show great promise as SIB electrodes because of their high electron conductivity, potential as backbone to support other active materials, easy production at the industrial-scale, and cost-effectiveness.[12–14]

However, these fibers have high contact resistance at the junctions, leading to a prolonged charge transfer path, which causes poor cycling stability and limits their further improvement in energy storage performances,[12] especially for SIBs with large Na^+ radius and sluggish Na-ion transport. Therefore, it is a great challenge to achieve fibers with adequate cyclability for Na-storage. Researchers have attempted to introduce graphene or carbon nanotubes into the fibers to enhance cycle performance.[15,16] To the best of our knowledge, there are very few reports on eliminating the contact resistance of carbon fibers for achieving better cycling performance, which is important for basic studies and industrial production of SIBs.

Eliminating the contact resistance requires fusing the fiber junctions, which is still a challenge for 1D materials.[17–19] Cheng *et al.* merged the junctions *via* carbonization of electrospun PAN/PVP/TPA hybrid composite fibers, which resulted in reduced electrical resistance and enhanced electrochemical energy storage properties.[12] However, the formation of fused fibers is largely affected by the solvent evaporation rate, need for heating power and a relatively humidity of 10–20% in the electrospinning chamber. An *et al.* achieved a junctioned copper fiber film through electrospinning and electroplating, which dramatically reduced the contact resistance at the junctions.[17] Thermal post-processing or mechanical pressing was also reported to merge the junctions.[20,21] However, these methods are complicated and not practical for low-cost materials.

It is crucial to improve mass transfer in the carbonization process for fusing the fiber junctions. The mass transfer can be accelerated by producing a highly active solid phase interface. In the present study, we provide a new strategy to fuse the fiber junctions for reducing the contact resistance. Herein, we introduce MoO_2 in the carbon fibers to replace the C–C interface

[a]State Key Laboratory of New Ceramics and Fine Processing, School of Materials Science and Engineering, Tsinghua University, Beijing 100084, P. R. China. E-mail: zhhuang@tsinghua.edu.cn

[b]Key Laboratory of Advanced Materials (MOE), School of Materials Science and Engineering, Tsinghua University, Beijing 100084, P. R. China

† Electronic supplementary information (ESI) available: Includes 8 pages containing 2 equations, 5 tables and 1 figure. See DOI: 10.1039/c8ra01908h

by the more active C–MoO_2–C interface at the fiber junction. During the carbonization process, MoO_2 reacts with the C matrix to generate Mo_2C, which promotes the mass transfer; this in turn results in the fusing of the fiber junctions. The fused junctions effectively reduce the contact resistance at the junctions, resulting in fast charge and ionic transport. Compared with the non-fused C fiber film, the self-fused C–Mo_2C fiber film exhibits excellent flexibility and much better cyclability with a capacity retention of 90% after 2000 cycles at a constant current density of 1 A g^{-1}.

2. Experimental section

2.1 Material synthesis

In a typical synthesis, 1.5 g polyacrylonitrile (PAN) and 0.3 g hexaammoniumheptamolybdate tetrahydrate were dissolved in 18 g dimethylformamide (DMF). The obtained mixture solution was electrospun at 1 ml h^{-1} and 25 kV (Fig. 1a). After electrospinning, the obtained fiber film was pre-oxidation in air at 170 °C for 12 h (Fig. 1b), in which PAN can be oxidized and then stable in air, followed by carbonization at 800 °C for 5 h in an Ar atmosphere (Fig. 1d). For comparison, a pure C fiber film was also prepared without adding hexaammoniumheptamolybdate tetrahydrate in DMF.

2.2 Characterizations

Crystal structures of the samples were examined by X-ray diffraction (XRD, Bruker D8-ADVANCE) under an accelerating voltage of 40 kV. Morphologies and structures were characterized by scanning electron microscopy (SEM, Dual-beam FIB 235, FEI Strata) and transmission electron microscopy (TEM, JEM-2100F, JEOL). Chemical compositions and structures were analyzed using X-ray photoelectron spectroscopy (XPS, ESCALAB 250Xi). The weight percentage of Mo_2C was determined by thermogravimetric analysis (TGA, Mettler Toledo TGA/DSC1) under air at a heating rate of 10 °C min^{-1}. N_2 adsorption studies were carried out at 77 K on the BELSORP-mini II system. The specific surface area and pore size distribution were analyzed by Brunauer–Emmett–Teller and nonlocal density functional theory method, respectively. Raman spectra were obtained using laser excitation at 532 nm (Renishaw, InVia-Reflex).

2.3 Electrochemical testing

The electrochemical performance was evaluated by using coin-type cells. The C–Mo_2C and C fiber films were used as the working electrodes without any additives or binders. A sodium foil and Whatman GF/A glass fiber were used as the counter electrode and separator, respectively. $NaClO_4$ (1 M) dissolved in an EC/DEC (1 : 1 by volume ratio) solution was used as the electrolyte. The cells were assembled in an argon-filled glove box where the concentrations of moisture and oxygen were maintained below 0.1 ppm. Electrochemical measurements were carried out after 24 h of battery assembly. The galvanostatic charge/discharge experiments were tested in the voltage range of 0.01–3 V at various current densities ranging from 20 to 5000 mA g^{-1} using the Land battery testing system (Jinnuo Electronics Co., Wuhan, China). Cyclic voltammetry (CV) and electrochemical impedance spectroscopy (EIS) measurements were obtained using an electrochemical workstation (VMP3, Bio-Logic). CV curves were tested in the potential range of 0.01–3 V at a scan rate of 0.5 mV s^{-1}. EIS measurements were carried out at an AC amplitude of 10 mV in the frequency range from 100 kHz to 0.01 Hz.

3. Results and discussions

Fig. 2a shows the XRD patterns of the C–Mo_2C and C fiber films after carbonization at 800 °C. For the C fiber film, there are two broad diffraction peaks at around 23° and 44° corresponding to

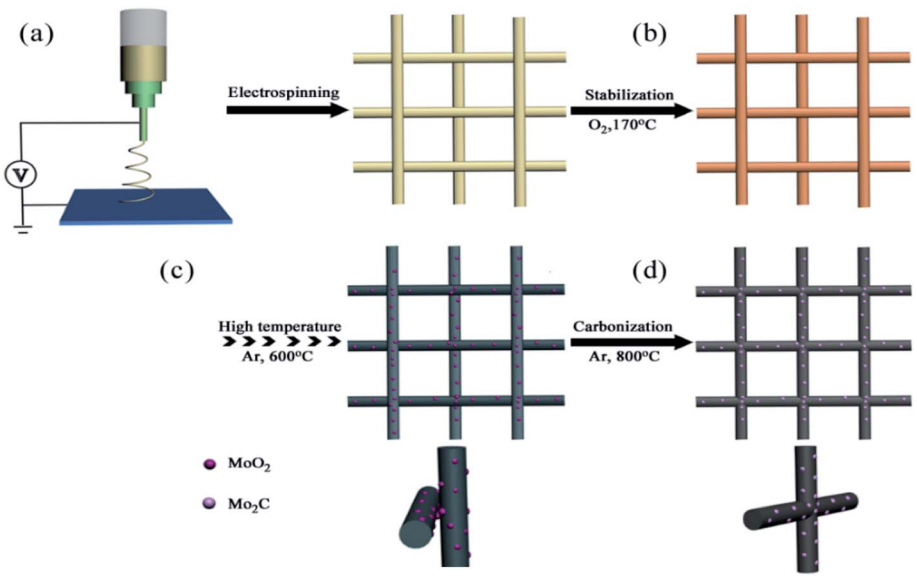

Fig. 1 Schematic illustration of the preparation process of the self-fused C–Mo_2C fiber film.

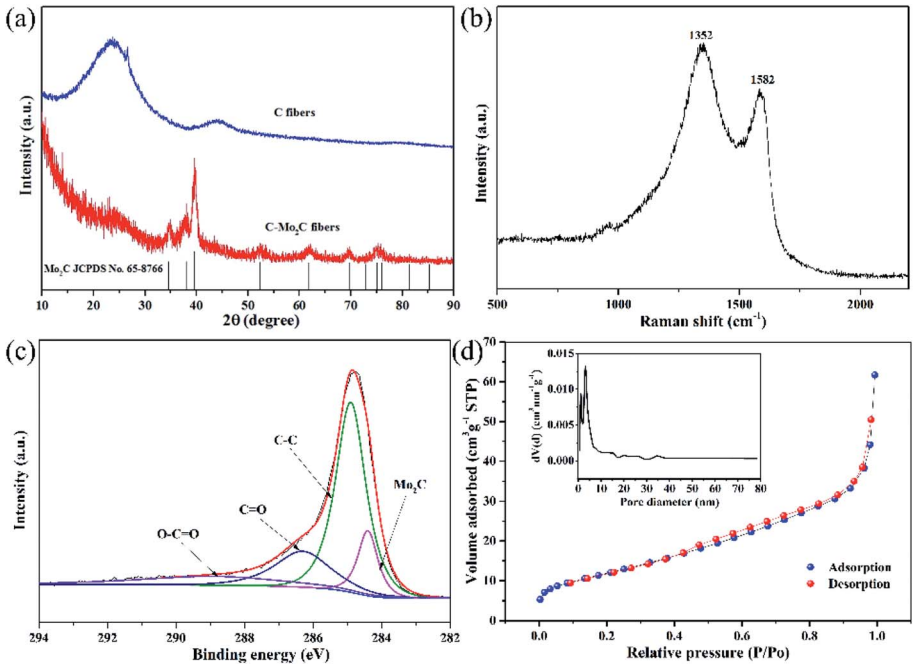

Fig. 2 (a) XRD patterns of C–Mo_2C and C fiber films; (b) Raman spectrum of the C–Mo_2C fiber film; (c) C 1s XPS spectra of the C–Mo_2C fiber film; (d) N_2 adsorption–desorption isotherms of the C–Mo_2C fiber film. The inset shows the corresponding pore size distribution curve.

amorphous carbon. In the case of the C–Mo_2C fiber film, the characteristic peaks of amorphous carbon as well as Mo_2C with the space group of $P6_3/mmc$ (JCPDS no. 65-8766) are seen. Besides, the diffraction peak of amorphous carbon is weaker relative to that of the C fiber film. This can be due to the fact that some of the amorphous carbon transforms into a crystalline product (Mo_2C) by reaction with MoO_2. Fig. 2b shows the Raman spectrum of the C–Mo_2C fiber film, with two intense

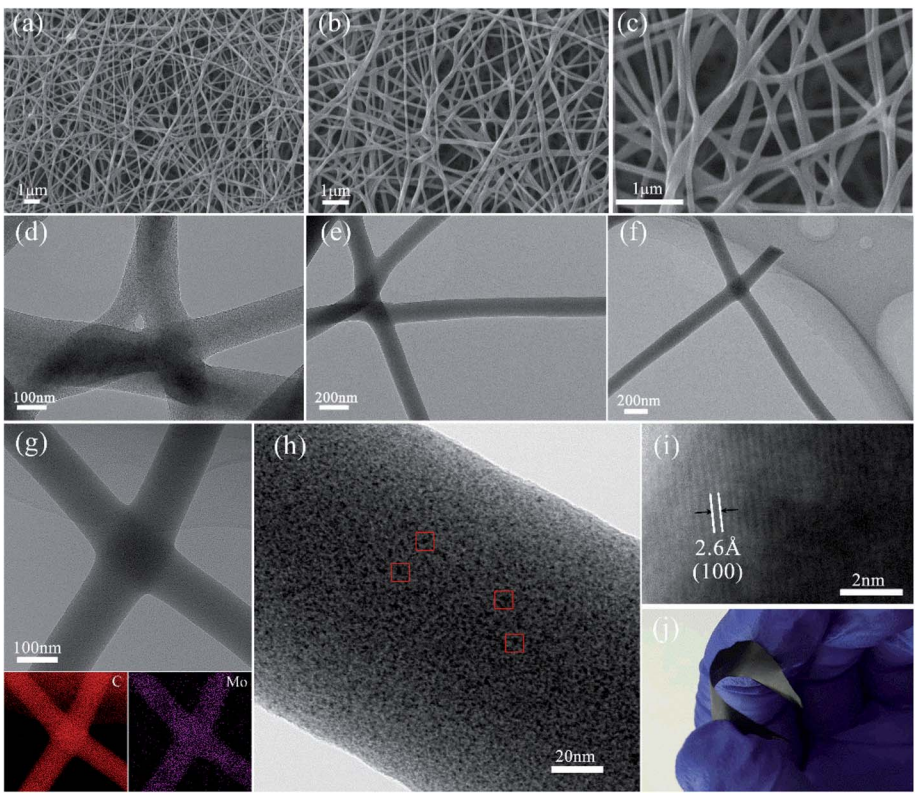

Fig. 3 (a–c) SEM images, (d–f) TEM images, (g) TEM (C and Mo) elemental mapping images, (h) TEM image, (i) HRTEM image, and (j) a photograph showing flexibility of the C–Mo_2C fiber film. (g) The magnification of the fiber junction in (f).

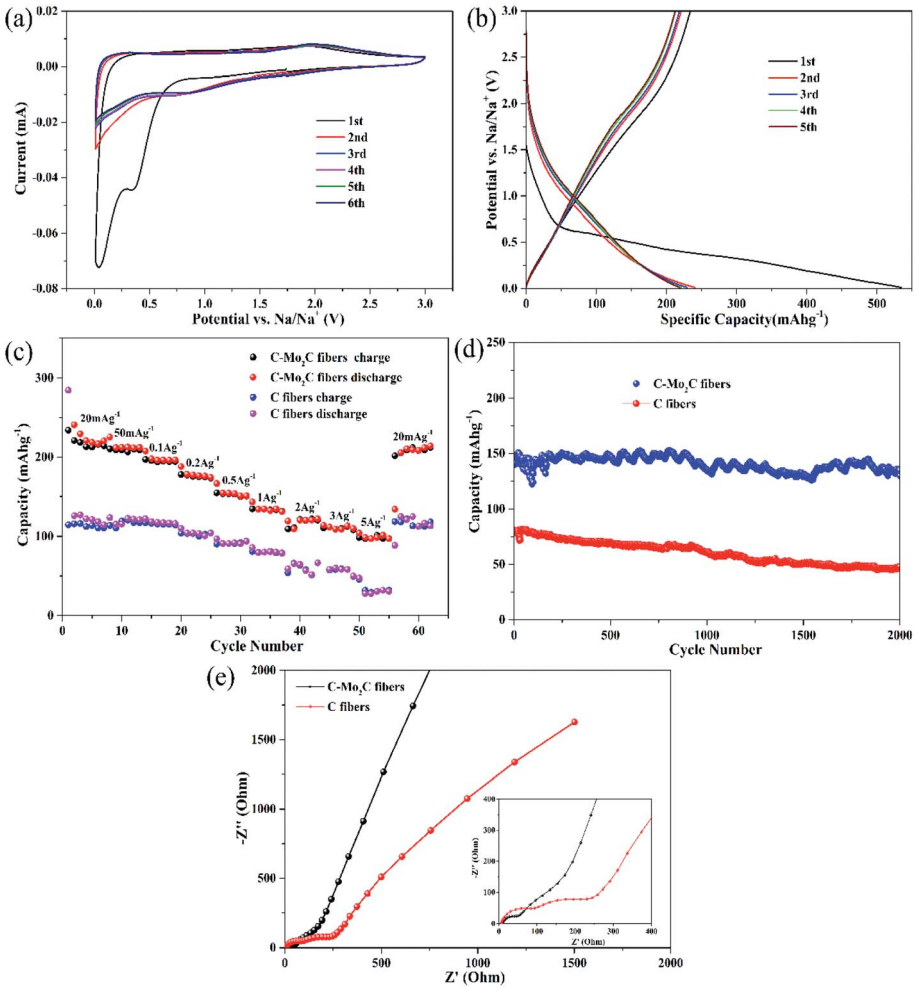

Fig. 4 Electrochemical performances of the C–Mo_2C and C fiber films as the anode electrodes of SIBs. (a) CV curves of the C–Mo_2C fiber film at a scan rate of 0.5 mV s^{-1}; (b) charge/discharge curves of the C–Mo_2C fiber film for the initial three cycles at 20 mA g^{-1}; (c) rate capabilities of C–Mo_2C and C fiber films; (d) cycling performances of C–Mo_2C and C fiber films at 1 A g^{-1}; (e) EIS curves of C–Mo_2C and C fiber films.

peaks at 1352 and 1582 cm^{-1} corresponding to the D band and G bands of carbon.[22,23] This suggests that the amorphous carbon matrix is derived from the decomposition of PAN. Fig. 2c shows the C 1s XPS spectra of the C–Mo_2C fiber film. The peak at 284.4 eV corresponds to the C–Mo bonds in Mo_2C, whereas the other peaks at 284.9, 286.3, and 288.9 eV correspond to the C–C, C=O, and O–C=O bonds.[24,25] Fig. 2d shows the N_2 adsorption–desorption isotherms of the C–Mo_2C fiber film; from the results, we can infer that it has a specific surface area of 44 m^2 g^{-1} and pore diameters of ~1.1 and ~3.1 nm. In addition, the curve also shows some weak peaks between 20 and 35 nm, indicating the presence of few mesopores with diameters in the range of 20–35 nm.

Fig. 3 shows the morphology and microstructure of the C–Mo_2C fiber film. The fibers with a diameter of 50–160 nm are randomly distributed and intersect to form a 3D reticular network, which retains the shape of the electrospun precursor fiber but is finer (Fig. S1†). The SEM and TEM images clearly show that the fiber junctions are fused with the aid of MoO_2. In contrast, the fiber junctions are not fused in the pure C fiber film (Fig. S3†). It is crucial to improve the mass transfer during the carbonization process for fusing the fiber junctions. Amorphous carbon reacts easily with MoO_2 because of lower activation energy of the reaction when compared with that of a reaction between amorphous carbons. $(NH_4)_6Mo_7O_{24}\cdot 4H_2O$ in the precursor fiber is decomposed into MoO_2 above 600 °C and forms highly active C–MoO_2–C interface at the fiber junction (Fig. 1c and S2†). When carbonized at 800 °C, MoO_2 reacts with the C matrix to generate Mo_2C at the C–MoO_2–C interface, which increases the mass transfer, leading to the fusing of fiber junctions. To study the distribution of Mo species (Mo_2C), energy dispersive X-ray spectroscopy (EDS) mapping was performed, as shown in Fig. 3g, which confirmed that molybdenum is uniformly distributed in the carbon fiber. Fig. 3h shows that Mo_2C particles with size of 2–4 nm were dispersed uniformly on the carbon fiber (marked by red squares). The high-resolution TEM image revealed a set of lattice fringes with an interplane spacing of 2.6 Å, which corresponded to the (100) plane of hexagonal Mo_2C (Fig. 4i). Due to the fused fiber junctions, the C–Mo_2C fiber film showed excellent flexibility, which was better than that of the C fiber film, as shown in Fig. 3j and Movie S1.†

Fig. 4 shows electrochemical performances of the C–Mo_2C and C fiber films as anodes of SIBs. The free-standing C–Mo_2C and C fiber films are directly used as the working electrodes without additives and binders. Fig. 4a shows the cyclic voltammetry (CV) curves of the C–Mo_2C fiber film with the first six cycles in the potential range of 0.01–3 V (*vs.* Na/Na^+) at a scan rate of 0.5 mV s^{-1}. In the first cathodic scan, a broad peak at 0.3 V corresponds to the formation of a solid electrolyte interface (SEI).[26,27] In the subsequent cycles, the broad peak around 0.9 V can be due to the conversion reactions between Mo_2C and Na^+. In the anodic process, the peak around 1.9 V is assigned to the extraction of Na^+ from Mo_2C. Fig. 4b shows the discharge/charge curves of the C–Mo_2C fiber film at a current density of 20 mA g^{-1} between 0.01 and 3 V *versus* Na/Na^+. The initial discharge and charge capacities are 534.6 and 233.9 mA h g^{-1}, respectively, leading to a limited initial coulombic efficiency (CE) of 43.8%. The huge capacity drop between the first two cycles can be due to the irreversible processes such as SEI formation, decomposition of electrolyte molecules, and trapping of some sodium in the lattice of Mo_2C. From the third cycle onwards, CE is higher than 95%, implying high reversibility and stability. The discharge/charge curves of the C fiber film have a CE of 40.3%, which is close to the value for the C–Mo_2C fiber film (Fig. S4†). Fig. 4c shows the rate capabilities of C–Mo_2C and C fiber films. The C–Mo_2C fiber film exhibits higher discharge capacities than the C fiber film under different current densities. The C–Mo_2C fiber film exhibits capacities of 212, 134, and 99 mA h g^{-1}, whereas the C fiber film shows low values of 121, 80, and 30 mA h g^{-1} at current densities of 50, 1000, and 5000 mA g^{-1}, respectively. Fig. 4d shows the cycling performance at a current density of 1 A g^{-1}. The C–Mo_2C fiber film exhibits high capacity retention of 90% after 2000 cycles. However, the capacity retention of the C fiber film is 60%. Fig. 4e shows the electrochemical impedance spectroscopy (EIS) curves for C–Mo_2C and C fiber films. The C–Mo_2C fiber film shows a much lower charge transfer resistance and sodium diffusion resistance when compared with the C fiber film. This reveals that the fused fiber junctions can dramatically reduce the contact resistance of the fibers, which is beneficial for both fast ionic and electronic transport, resulting in excellent cycling stability and high capacity. Additionally, the Mo_2C particles provide many electrochemically active sites, leading to additional improvement in sodium storage.

4. Conclusion

In summary, we have presented a new approach to fuse fiber junctions by introducing MoO_2, which results in the formation of a highly active C–MoO_2–C interface at the fiber junction, and this promotes mass transfer. The fused junction eliminates the contact resistance at the fiber junctions, and this can significantly accelerate the ion/electron transport. Therefore, the self-fused C–Mo_2C fiber film shows excellent flexibility and high electrochemical performance. This approach opens up a vast array of new opportunities in flexible high-performance batteries and other low-cost, large-area energy storage devices.

Conflicts of interest

There are no conflicts to declare.

Acknowledgements

This study was supported by the National Natural Science Foundation of China (grant no. 51672151) and 973 Program of China (No. 2014CB932401).

References

1 N. Yabuuchi, K. Kubota, M. Dahbi and S. Komaba, *Chem. Rev.*, 2014, **114**, 11636–11682.
2 M. D. Slater, D. Kim, E. Lee and C. S. Johnson, *Adv. Funct. Mater.*, 2013, **23**, 947–958.
3 S.-W. Kim, D.-H. Seo, X. Ma, G. Ceder and K. Kang, *Adv. Energy Mater.*, 2012, **2**, 710–721.
4 V. Palomares, P. Serras, I. Villaluenga, K. B. Hueso, J. Carretero-Gonzalez and T. Rojo, *Energy Environ. Sci.*, 2012, **5**, 5884–5901.
5 M. D. Slater, D. Kim, E. Lee and C. S. Johnson, *Adv. Funct. Mater.*, 2013, **23**, 947–958.
6 P. Barpanda, T. Ye, S.-i. Nishimura, S.-C. Chung, Y. Yamada, M. Okubo, H. Zhou and A. Yamada, *Electrochem. Commun.*, 2012, **24**, 116–119.
7 S. Komaba, W. Murata, T. Ishikawa, N. Yabuuchi, T. Ozeki, T. Nakayama, A. Ogata, K. Gotoh and K. Fujiwara, *Adv. Funct. Mater.*, 2011, **21**, 3859–3867.
8 P.-c. Tsai, S.-C. Chung, S.-k. Lin and A. Yamada, *J. Mater. Chem. A*, 2015, **3**, 9763–9768.
9 K. Tang, L. Fu, R. J. White, L. Yu, M. M. Titirici, M. Antonietti and J. Maier, *Adv. Energy Mater.*, 2012, **2**, 873–877.
10 S. Wenzel, T. Hara, J. Janek and P. Adelhelm, *Energy Environ. Sci.*, 2011, **4**, 3342–3345.
11 Y. Yan, Y. X. Yin, Y. G. Guo and L. J. Wan, *Adv. Energy Mater.*, 2014, **4**, 1301584–1301588.
12 Y. Cheng, L. Huang, X. Xiao, B. Yao, L. Yuan, T. Li, Z. Hu, B. Wang, J. Wan and J. Zhou, *Nano Energy*, 2015, **15**, 66–74.
13 C. Lai, Z. Zhou, L. Zhang, X. Wang, Q. Zhou, Y. Zhao, Y. Wang, X.-F. Wu, Z. Zhu and H. Fong, *J. Power Sources*, 2014, **247**, 134–141.
14 Z. Tai, X. Yan, J. Lang and Q. Xue, *J. Power Sources*, 2012, **199**, 373–378.
15 B. Zhang, J. Huang and J. K. Kim, *Adv. Funct. Mater.*, 2015, **25**, 5222–5228.
16 J. Zhu, G. Zhang, X. Yu, Q. Li, B. Lu and Z. Xu, *Nano Energy*, 2014, **3**, 80–87.
17 S. An, H. S. Jo, D.-Y. Kim, H. J. Lee, B.-K. Ju, S. S. Al-Deyab, J.-H. Ahn, Y. Qin, M. T. Swihart, A. L. Yarin and S. S. Yoon, *Adv. Mater.*, 2016, **28**, 7149–7154.
18 P. C. Hsu, S. Wang, H. Wu, V. K. Narasimhan, D. S. Kong, H. R. Lee and Y. Cui, *Nat. Commun.*, 2013, **4**, 2522–2528.

19 H. Wu, D. S. Kong, Z. C. Ruan, P. C. Hsu, S. Wang, Z. F. Yu, T. J. Carney, L. B. Hu, S. H. Fan and Y. Cui, *Nat. Nanotechnol.*, 2013, **8**, 421–425.
20 W. Gaynor, G. F. Burkhard, M. D. McGehee and P. Peumans, *Adv. Mater.*, 2011, **23**, 2905–2910.
21 E. C. Garnett, W. S. Cai, J. J. Cha, F. Mahmood, S. T. Connor, M. G. Christoforo, Y. Cui, M. D. McGehee and M. L. Brongersma, *Nat. Mater.*, 2012, **11**, 241–249.
22 Y. Xiao, P. Sun and M. Cao, *ACS Nano*, 2014, **8**, 7846–7857.
23 Y. Xiao, L. Zheng and M. Cao, *Nano Energy*, 2015, **12**, 152–160.
24 R. Li, S. Wang, W. Wang and M. Cao, *Phys. Chem. Chem. Phys.*, 2015, **17**, 24803–24809.
25 Q. Gao, X. Y. Zhao, Y. Xiao, D. Zhao and M. H. Cao, *Nanoscale*, 2014, **6**, 6151–6157.
26 L. David, R. Bhandavat and G. Singh, *ACS Nano*, 2014, **8**, 1759–1770.
27 J. Zhang, D.-W. Wang, W. Lv, S. Zhang, Q. Liang, D. Zheng, F. Kang and Q.-H. Yang, *Energy Environ. Sci.*, 2017, **10**, 370–376.